Monthly Notices of the ROYAL ASTRONOMICAL SOCIETY

MNRAS **545,** 1–11 (2026) https://doi.org/10.1093/mnras/staf2081
Advance Access publication 2025 November 22

Subgrid modelling of MRI-driven turbulence in differentially rotating neutron stars

Miquel Miravet-Tenés [1,2]★ Martin Obergaulinger [2,3] Pablo Cerdá-Durán [2,3] José A. Font [2,3] and Milton Ruiz [2]

[1]*Mathematical Sciences and STAG Research Centre, University of Southampton, Southampton SO17 1BJ, UK*
[2]*Departament d'Astronomia i Astrofísica, Universitat de València, C/ Dr Moliner 50, E-46100 Burjassot (València), Spain*
[3]*Observatori Astronòmic, Universitat de València, C/ Catedrático José Beltrán 2, E-46980 Paterna (València), Spain*

Accepted 2025 November 18. Received 2025 November 18; in original form 2025 September 19

ABSTRACT

Following a binary neutron star (BNS) merger, the transient remnant is often a fast spinning, differentially rotating, magnetized hypermassive neutron star (HMNS). This object is prone to the magnetorotational instability (MRI) which drives magnetohydrodynamic turbulence that significantly influences the HMNS global dynamics. A key consequence of turbulence is the outward transport of angular momentum which impacts the remnant's stability and lifetime. Most numerical simulations of BNS mergers are unable to resolve the MRI due to its inherently small wavelength. To overcome this limitation, subgrid models have been proposed to capture the effects of unresolved small-scale physics in terms of large-scale quantities. We present the first implementation of our MHD-Instability-Induced Turbulence (MInIT) model in global Newtonian simulations of MRI-sensitive, differentially rotating, magnetized neutron stars. Here, we show that by adding the corresponding turbulent stress tensors to the momentum equation, MInIT successfully reproduces the angular momentum transport in neutron stars driven by small-scale turbulence.

Key words: MHD – Turbulence – Stars: neutron.

1 INTRODUCTION

Multimessenger observations of binary neutron star (BNS) mergers provide the most direct evidence that stellar compact mergers, where at least one of the binary companions is a neutron star (NS), may be progenitors of the central engines that power gamma-ray bursts (GRBs) (A. I. MacFadyen & S. E. Woosley 1999; M. Ruiz et al. 2016; B. P. Abbott et al. 2017b, c). They also give strong observational support to theoretical proposals linking BNS mergers with production sites for r-process nucleosynthesis and kilonovae (D. Eichler et al. 1989; L.-X. Li & B. Paczynski 1998; B. D. Metzger et al. 2010). Moreover, they can be used as standard sirens to give an independent measure of the expansion of the Universe (B. F. Schutz 1986; S. Nissanke et al. 2010; B. P. Abbott et al. 2017a), and help put tight constraints on the equation of state (EOS) of matter at supranuclear densities (see e.g. B. Margalit & B. D. Metzger 2017; M. Shibata et al. 2017; L. Rezzolla, E. R. Most & L. R. Weih 2018; M. Ruiz, S. L. Shapiro & A. Tsokaros 2018, and references therein).

After merger, the system settles down into a new configuration. The merger outcome strongly depends on the total mass of the system and on the EOS considered (see e.g. A. L. Piro, B. Giacomazzo & R. Perna 2017; S. Bernuzzi 2020; N. Sarin & P. D. Lasky 2021, for reviews). If the total mass of the remnant is somewhat larger than the mass of a stationary non-rotating NSs [Tolman–Oppenheimer–Volkoff (TOV) solutions with mass $M_{\rm TOV}$], the system may go through a phase in which a transient post-merger object forms, a so-called hypermassive neutron star (HMNS), supported against gravitational collapse by rapid differential rotation and thermal pressure.[1] The maximum mass of these remnants depends on the EOS (T. W. Baumgarte, S. L. Shapiro & M. Shibata 2000; M. Shibata et al. 2006; A. Bauswein, T. W. Baumgarte & H. T. Janka 2013; A. L. Piro et al. 2017; L. R. Weih, E. R. Most & L. Rezzolla 2018; P. L. Espino & V. Paschalidis 2019). The HMNS may survive for several tens (or even hundreds) of milliseconds, undergoing oscillations and magnetohydrodynamic (MHD) instabilities, and ejecting mass that forms a disc around the bulk of the star. Both the rotational profile and the disc mass depend on the EOS (e.g. W. Kastaun & F. Galeazzi 2015) and the mass ratio of the binary system (e.g. S. Bernuzzi 2020). Massive NS remnants, apart from being differentially rotating, are characterized by strong magnetic fields (up to $B \sim 10^{16}$ G, e.g. K. Kiuchi et al. 2014; C. Palenzuela et al. 2022). Such large values are the result of amplification periods both during and after merger, due to MHD instabilities such as the Kelvin–Helmholtz instability (KHI), when the NSs are merging (e.g. M. Anderson et al. 2008; Y. T. Liu et al. 2008; K. Kiuchi et al. 2015; C. Palenzuela et al. 2022), and the magnetorotational instability (MRI), during the post-merger phase

[1]Temperatures in BNS mergers may be ~ 100 MeV and the inclusion of thermal effects in the EOS is needed (A. Perego, S. Bernuzzi & D. Radice 2019; P. Hammond, I. Hawke & N. Andersson 2021).

★ E-mail: m.miravet-tenes@soton.ac.uk

© The Author(s) 2025.
Published by Oxford University Press on behalf of Royal Astronomical Society. This is an Open Access article distributed under the terms of the Creative Commons Attribution License (https://creativecommons.org/licenses/by/4.0/), which permits unrestricted reuse, distribution, and reproduction in any medium, provided the original work is properly cited.

Downloaded from https://academic.oup.com/mnras/article/545/3/staf2081/8340377 by guest on 12 January 2026

(e.g. K. Kiuchi et al. 2014, 2018, 2024; M. Ruiz et al. 2016; T. Kawamura et al. 2016).

Once support against gravity by rapid rotation and thermal pressure diminishes, the remnant eventually collapses to a black hole. Damping of differential rotation comes from magnetic and viscous dissipation, i.e. angular momentum transport, that may arise from instabilities such as the MRI (S. A. Balbus & J. F. Hawley 1998; S. L. Shapiro 2000; M. D. Duez et al. 2004, 2006, 2020; M. Shibata & Y.-I. Sekiguchi 2005; D. M. Siegel et al. 2013; B. Margalit et al. 2022). It is also worth mentioning that the stability of protoneutron stars, which also exhibit rapid differential rotation at birth, can be also influenced by the development of the MRI (e.g. S. Akiyama et al. 2003; M. Obergaulinger et al. 2006; P. Cerdá-Durán et al. 2008; T. Rembiasz et al. 2016a, b; A. Reboul-Salze et al. 2021). Ionized rotating fluids with angular frequency profiles decreasing outwards are particularly unstable to the MRI (E. P. Velikhov 1959; S. Chandrasekhar 1960; S. A. Balbus & J. F. Hawley 1991) when threaded by a weak magnetic field in the direction perpendicular to the shear. Seed perturbations can grow exponentially on time-scales close to the rotational period. These perturbations take the form of the so-called 'channel modes', which are pairs of vertically stacked layers in which the velocity and the magnetic field perturbations have radial and azimuthal components of (sinusoidally) alternating polarity. These modes have associated Maxwell and Reynolds stresses that lead to outward transport of angular momentum (J. Goodman & G. Xu 1994; M. E. Pessah, C.-K. Chan & D. Psaltis 2006; M. E. Pessah & C.-k. Chan 2008). The MRI possesses a critical wavelength, $\lambda_{\rm MRI} \approx 2\pi v_{\rm A}/\Omega$ (e.g. M. Shibata 2015), which scales with the Alfvén speed $v_{\rm A}$ and the rotation frequency of the fluid Ω, and corresponds to the fastest growing mode. In the context of BNS mergers, simulations focus on solving this mode (D. M. Siegel et al. 2013; K. Kiuchi et al. 2018; R. Ciolfi et al. 2019; K. Kiuchi et al. 2024). However, this spatial scale is typically of the order of only tens of metres, making it challenging to resolve the MRI in numerical simulations of BNS systems.

The exponential growth of the instability eventually terminates. The laminar MRI channel flows can be unstable against parasitic instabilities (PIs) (J. Goodman & G. Xu 1994; H. N. Latter, P. Lesaffre & S. A. Balbus 2009; P. Lesaffre, S. A. Balbus & H. Latter 2009; M. Miravet-Tenés & M. E. Pessah 2025) that can be of KH or tearing mode type, depending on the value of kinematic viscosity and resistivity, i.e. non-ideal effects (M. E. Pessah & J. Goodman 2009; M. E. Pessah 2010). These secondary instabilities initially grow slowly, but eventually they evolve faster than the MRI modes, since their growth rate is exponential to the MRI amplitude. When both primary and secondary instabilities reach a similar amplitude, the channel modes are disrupted and the MRI saturates (T. Rembiasz et al. 2016a, b), leading to a turbulent regime.

Numerical simulations of astrophysical systems such as BNS mergers, neutron star–black hole (NSBH) mergers, and core-collapse supernovae are inherently challenging due to the complex and multifaceted physics involved. One key issue is capturing small-scale turbulence (e.g. D. Radice & I. Hawke 2024). The prohibitive spatial resolution required to resolve all scales prevents general relativistic magnetohydrodynamics (GRMHD) simulations from properly describing the turbulence triggered by MHD instabilities. An emerging alternative is the use of large-eddy simulations (LES), which have already been employed to simulate both BNS and NSBH mergers (B. Giacomazzo et al. 2015; D. Radice 2020; C. Palenzuela et al. 2022; R. Aguilera-Miret, D. Viganò & C. Palenzuela 2022; M. R. Izquierdo et al. 2024). This approach aims to model, through the application of a subgrid closure, the small-scale turbulence in terms of resolved quantities. More precisely, LES provide a closure for the turbulent stress tensors, which appear in the spatially filtered non-linear mean-field MHD equations. The approach of LES is very similar to that of the Reynolds-averaged Navier–Stokes equations, where flow quantities are decomposed into their time-averaged and rapidly fluctuating components. In this approach, only the mean flow is resolved, as opposed to the rapidly varying fluctuations which are subject to a closure model (O. Reynolds 1895; P. Y. Chou 1945). In contrast, LES are able to capture the largest turbulent spatial scales, but not the entire inertial range of scales.

In M. Miravet-Tenés et al. (2022, 2024), we presented a new Newtonian subgrid model for MHD turbulence triggered by the MRI and the KHI, the dominant MHD instabilities in BNS mergers. The model, dubbed MHD-Instability-Induced-Turbulence (MInIT), is based on evolution equations for the turbulent kinetic energy densities. These equations are built using phenomenological arguments that are physically motivated. The turbulent densities are connected to the stress tensors through certain calibrated coefficients. This model allows handling delays in the growth of the instability and the decay of turbulence, and it has been calibrated by fully resolved local numerical simulations. Moreover, it has been adapted to the instabilities that are key drivers of turbulence in BNS mergers, in contrast to other models already applied to LES, which are only able to partially capture the magnetic field amplification driven by the KHI, but do not show any evidence of MRI development. The gradient model employed in, e.g. C. Palenzuela et al. (2022) and R. Aguilera-Miret et al. (2025), seems to provide promising results when dealing with partially resolved turbulence, as in the case of the KHI, since the model seems to extrapolate the turbulent cascade to the unresolved small scales. However, there is no evidence that this model is able to capture the impact of subgrid turbulence triggered by the MRI, because this instability is expected to fully develop in the unresolved scales.

In this work, we use the MInIT model in global Newtonian simulations of MRI-sensitive, differentially rotating, magnetized NSs and evaluate its capability to accurately resolve the MRI dynamics. We focus on the angular momentum transport arising from the inclusion of subgrid terms in the momentum equation, deferring to a future work the effect of the subgrid scales on the expected magnetic field amplification after MRI saturation. By exploring different rotational frequencies, magnetic field strengths, and initial values of the turbulent energy densities, we study their impact on the angular momentum transport time-scale in simulations that lack enough spatial resolution to directly resolve the MRI.

This paper is organized as follows: in Section 2 we introduce the mean-field MHD equations with the inclusion of the turbulent stresses. We describe in Section 3 the closure model for turbulence we employ in the simulations. The numerical methodology is discussed in Section 4 and the results are showcased in Section 5. Conclusions are drawn in Section 6, along with prospects for future research. Finally, Appendix A discusses the effect numerical dissipation might have in our simulations. Unless otherwise stated we employ cgs units. Latin indices run from 1 to 3.

2 MEAN-FIELD MHD EQUATIONS

We start by briefly reviewing the Newtonian ideal MHD equations which form the mathematical framework for our study. These equations couple the different variables of a plasma, such as the gas

Downloaded from https://academic.oup.com/mnras/article/545/3/staf2081/8340377 by guest on 12 January 2026

pressure, the mass density, the velocity, and the magnetic field. We can express this system of equations as

$$\partial_t \rho + \nabla_j \left[\rho v^j\right] = 0, \tag{1}$$

$$\partial_t p^i + \nabla_j \left[p^i v^j + P_\star \delta^{ij} - b^i b^j\right] = f^i, \tag{2}$$

$$\partial_t e_\star + \nabla_j \left[(e_\star + P_\star) v^j - b^i v_i b^j\right] = f^j v_j, \tag{3}$$

$$\partial_t \vec{b} = -c\vec{\nabla} \times \vec{E}, \tag{4}$$

$$\nabla_j b^j = 0\,, \tag{5}$$

where ρ is the mass density, v^i are the components of the fluid velocity, b^i are the magnetic field components, $p^i = \rho v^i$ is the momentum density, $P_\star = P_{\rm gas} + b^2/2$ is the total pressure, $e_\star = e_{\rm int} + \rho v^2/2 + b^2/2$ is the total energy density, and f^i is an external force density, which, in this case, corresponds to gravity, $f_i = -\rho \nabla_i \Phi$. The gravitational potential Φ is computed as

$$\Phi(r) = -4\pi \int_0^\infty {\rm d}r' r'^2 \frac{\rho}{|r - r'|}\,, \tag{6}$$

where r is the radial spherical coordinate. By applying the mean-field MHD formalism (F. Krause & K. Rädler 1980; M. Miravet-Tenés et al. 2022, 2024), the above system of equations can be expressed in terms of resolved and subgrid-scale terms. If we assume that the behaviour of a given field $\boldsymbol{A}$ is solved for a certain length scale l, we can introduce a spatial filter that acts on that scale. The residual between filtered and unfiltered fields will be the turbulent contribution

$$\boldsymbol{A'} = \boldsymbol{A} - \bar{\boldsymbol{A}}\,, \tag{7}$$

where the bar symbol denotes the filtering/averaging operator and the prime symbol is used to identify the turbulent field. This operation satisfies the Reynolds averaging rules and can be either a spatial filtering, as in our case, or a temporal averaging, acting on a time-scale τ (P. Charbonneau 2013). By introducing this decomposition in the MHD equations, which are non-linear, and after applying the filtering operation to the equations, additional terms with products of turbulent quantities will appear. By construction, the average of the turbulent contribution is zero. Thus, the only possible turbulent terms arising in the mean-field equations are the averaged products of two or more unresolved variables. Following M. Miravet-Tenés et al. (2022, 2024) we consider only fluctuations of the velocity and magnetic fields. Therefore, the filtered products of these unresolved variables can be represented by

$$\bar{M}_{ij} = \overline{b'_i b'_j}, \tag{8}$$

$$\bar{R}_{ij} = \overline{v'_i v'_j}, \tag{9}$$

$$\bar{F}_{ij} = \overline{v'_i b'_j} - \overline{v'_j b'_i}\,, \tag{10}$$

which correspond to the Maxwell, Reynolds, and Faraday turbulent stress tensors, respectively. Linear combinations of these terms will appear as effective source terms in the mean-field version of the system (1)–(5).

Since the aim of this work is to solely study angular momentum transport, we will focus on the mean-field form of the momentum equation,

$$\partial_t \bar{p}^i + \nabla_j \left[\bar{\rho}\bar{v}^i\bar{v}^j + \left(\bar{P}_\star + \frac{1}{2}{\rm Tr}\{\bar{\mathbf{M}}\}\right)\delta^{ij} - \bar{b}^i\bar{b}^j + \bar{\rho}\bar{R}^{ij} - \bar{M}^{ij}\right] = \bar{f}^i\,, \tag{11}$$

where the trace of the Maxwell stress can be regarded as a turbulent magnetic pressure. Density perturbations are neglected, i.e. $\bar{\rho} = \rho$, which leaves the continuity equation unchanged. For the sake of simplicity we do not include any subgrid term in the energy and induction equations. Therefore, we do not expect a turbulent dynamo that exponentially amplifies the large-scale magnetic field. A study of the effect of the MRI turbulent dynamo in the large-scale dynamics is deferred to future work.

3 THE MINIT MODEL FOR THE MRI

The turbulent stress tensors that appear in equation () need a closure relation, i.e. they need to be connected to the resolved variables in order to write the system of equations as a closed system amenable to be solved numerically. In the MInIT subgrid model (M. Miravet-Tenés et al. 2022) the closure relation is obtained by introducing a new quantity, the turbulent kinetic energy density, with an evolution equation of the form

$$\partial_t e_{\rm turb} + \nabla_j(\bar{v}_j e_{\rm turb}) = S^{\rm turb}\,, \tag{12}$$

where $S^{\rm turb}$ comprises source terms that depend on the specific kind of MHD turbulence under consideration. In the context of this work, the dominant MHD instability, and the one that will develop subgrid turbulence, is the MRI. As shown in M. Miravet-Tenés et al. (2022), the secondary PIs are responsible for the saturation of the MRI. Therefore, we need two evolution equations to account for the two instabilities, the MRI and the PI:

$$\partial_t e_{\rm MRI} + \nabla_j(\bar{v}_j e_{\rm MRI}) = 2\,\gamma_{\rm MRI}\,e_{\rm MRI} - 2\,\gamma_{\rm PI}\,e_{\rm PI}\,, \tag{13}$$

$$\partial_t e_{\rm PI} + \nabla_j(\bar{v}_j e_{\rm PI}) = 2\,\gamma_{\rm PI}\,e_{\rm PI} - S_{\rm TD}\,. \tag{14}$$

In the ideal MHD case, the explicit form of the MRI growth rate of the fastest-growing mode, $\gamma_{\rm MRI}$, is (S. A. Balbus & J. F. Hawley 1992; M. Obergaulinger et al. 2009)

$$\gamma_{\rm MRI} = \frac{q}{2}\Omega\,, \tag{15}$$

where Ω is the angular frequency of the fluid and q is known as the shear parameter

$$q \equiv -\frac{{\rm d}\ln\Omega}{{\rm d}\ln r}\,. \tag{16}$$

Correspondingly, the growth rate of the PIs can be expressed as (M. E. Pessah 2010; M. Miravet-Tenés et al. 2022)

$$\gamma_{\rm PI} = \sigma k_{\rm MRI}\sqrt{\frac{2e_{\rm MRI}}{\bar{\rho}}}\,, \tag{17}$$

with $\sigma = 0.27$ (M. E. Pessah 2010) and $k_{\rm MRI}$ being the wavenumber of the fastest growing MRI mode (T. Rembiasz et al. 2016a),

$$k_{\rm MRI} = \sqrt{1 - \frac{(2-q)^2}{4}}\,\frac{\Omega}{\bar{v}_{\rm Az}}\,, \tag{18}$$

where $\bar{v}_{\rm Az} = \bar{b}_z/\sqrt{\bar{\rho}}$ is the vertical component of the Alfvén velocity. In practice, since the vertical and poloidal components of the magnetic field are very similar in our simulations, we will use the latter to avoid divisions by zero at certain points of the domain. The growing term for the PI in equation (14), i.e. the source term with positive sign, acts as a sink for the MRI energy in equation (13), since the secondary instabilities feed off the main one. The sink term from equation (14), $S_{\rm TD}$, represents the dissipation of the turbulent kinetic energy into thermal energy at the end of the Kolmogorov scale, i.e.

Downloaded from https://academic.oup.com/mnras/article/545/3/staf2081/8340377 by guest on 12 January 2026

the inertial range of scales (L. D. Landau & E. M. Lifshitz 1987; M. Miravet-Tenés et al. 2022). It is given by

$$S_{\rm TD} = C\,\frac{e_{\rm PI}^{3/2}}{\sqrt{\bar{\rho}}\lambda}\,, \tag{19}$$

where $C = 8.6$, a value empirically found in M. Miravet-Tenés et al. (2022), and $\lambda = \min[\Delta, \lambda_{\rm MRI}]$, with Δ the numerical cell size and $\lambda_{\rm MRI}$ the wavelength of the fastest growing MRI mode, $\lambda_{\rm MRI} = 2\pi/k_{\rm MRI}$.

The stress tensors are linked to these turbulent energy densities through constant proportionality coefficients,

$$\bar{M}_{ij}(t,\boldsymbol{r}) = \alpha_{ij}^{\rm MRI}\, e_{\rm MRI}(t,\boldsymbol{r}) + \alpha_{ij}^{\rm PI}\, e_{\rm PI}(t,\boldsymbol{r})\,, \tag{20}$$

$$\bar{R}_{ij}(t,\boldsymbol{r}) = \frac{1}{\bar{\rho}(t,\boldsymbol{r})}\left(\beta_{ij}^{\rm MRI}\, e_{\rm MRI}(t,\boldsymbol{r}) + \beta_{ij}^{\rm PI}\, e_{\rm PI}(t,\boldsymbol{r})\right)\,, \tag{21}$$

$$\bar{F}_{ij}(t,\boldsymbol{r}) = \frac{\gamma_{ij}^{\rm PI}}{\sqrt{\bar{\rho}(t,\boldsymbol{r})}} e_{\rm PI}(t,\boldsymbol{r})\,, \tag{22}$$

which are either obtained from theoretical arguments (in the case of the MRI coefficients; M. E. Pessah & C.-k. Chan 2008) or calibrated using numerical box simulations (for the PI coefficients; M. Miravet-Tenés et al. 2022). The dominant contributions responsible for angular momentum transport in the momentum equation are the cylindrical $\varpi\phi$ components of the Maxwell and Reynolds stresses. Here, the quantity ϖ corresponds to the cylindrical radius, i.e. the distance to the rotation axis, $\varpi = r\sin\theta$. The coefficients corresponding to the MRI components are

$$\alpha_{\varpi\phi}^{\rm MRI} = 1 - 4/q\,, \tag{23}$$

$$\beta_{\varpi\phi}^{\rm MRI} = 1\,, \tag{24}$$

while the calibrated parasitic coefficients are $\alpha_{\varpi\phi}^{\rm PI} = -1.4$ and $\beta_{\varpi\phi}^{\rm PI} = -0.8$. Uncertainties (standard deviation) in these quantities arise from both the spatial and time averages performed over the simulation data in M. Miravet-Tenés et al. (2022). The rest of the coefficients can be found in M. Miravet-Tenés et al. (2022).

4 NUMERICAL APPROACH

4.1 Initial models

The differentially rotating initial equilibrium models are computed using the Newtonian version of the code described in H. Dimmelmeier, J. A. Font & E. Muller (2002), based on Hachisu's self-consistent field method (H. Komatsu, Y. Eriguchi & I. Hachisu 1989). The rotation law of the equilibrium model is given by

$$\Omega(\varpi) = \frac{\Omega_c}{1 + \frac{\varpi^2}{A^2}}\,, \tag{25}$$

where A is a positive constant and Ω_c is the value of Ω, the angular frequency, at the coordinate centre (H. Komatsu et al. 1989). In all our simulations, we set $A = 5$ km. In the limit where $A \to \infty$, the star becomes a rigid rotator. The initial values of the turbulent energy densities of the MRI and the PI will be a fraction of the total kinetic energy density (see Section 5.3).

Regarding the EOS, a polytropic relation between the pressure P and the rest-mass density ρ is employed for the initial equilibrium configuration:

$$P = K\rho^{\gamma}\,, \tag{26}$$

with $\gamma = 2$ and $K = 145529.19$ g^{-1} cm^5 s^{-2}. This means that the initial system has zero temperature. In the evolution, we use a hybrid approach by adding a thermal component to the polytropic EOS via an ideal-gas-like EOS (H. T. Janka, T. Zwerger & R. Moenchmeyer 1993; T. Zwerger & E. Mueller 1997):

$$P_{\rm th} = (\Gamma_{\rm th} - 1)\epsilon_{\rm th}\,, \tag{27}$$

where $\Gamma_{\rm th} = 1.33$ and $\epsilon_{\rm th}$ is the thermal energy density. Initially, both $\epsilon_{\rm th}$ and $P_{\rm th}$ should be zero in the absence of shocks (H. T. Janka et al. 1993), so it is natural to build an initial model at zero temperature.

A dipolar magnetic field is implemented as in Y. Suwa et al. (2007), with the following components of the effective vector potential (in a spherical coordinate system),

$$A_r = 0\,, \tag{28}$$

$$A_\theta = 0\,, \tag{29}$$

$$A_\phi = \frac{\bar{b}_0}{2}\frac{r_0^3}{r^3 + r_0^3}\varpi \times \max(0, (\rho - \rho_{\rm cut})/\rho_{\rm max})\,, \tag{30}$$

where r_0 and $\bar{b}_0$ are model constants, the latter being the value of the magnetic field at the centre of the star. In all our initial models we set $r_0 = 12$ km, being the equatorial radius of the star $R_{\rm eq} \approx 18.5$ km (see Table 1). The last factor in the expression for A_ϕ is included to (initially) keep the magnetic field confined inside the star (Z. B. Etienne et al. 2012; M. Ruiz, A. Tsokaros & S. L. Shapiro 2021). The cutoff density $\rho_{\rm cut}$ is a free parameter that confines the magnetic field within $\rho > \rho_{\rm cut}$. We set $\rho_{\rm cut}$ to 10 per cent of the initial maximum density, which corresponds to an equatorial radial distance of roughly 17 km for all simulations.

The polytropic EOS in equation (26) leads to a very steep density profile at the surface of the star. In order to deal with the vacuum region surrounding the star we use a low-density atmosphere, as customary in these kind of simulations, where the hydrodynamical variables are not evolved (see section 3.4. from H. Dimmelmeier et al. 2002). The threshold value of the mass density to characterize the atmosphere is set to $\rho_{\rm atm} = 10^9$ g cm^{-3}, which is roughly five orders of magnitude smaller than the initial central density of the star (see Table 1). The rapid decrease of the density with the radial distance can lead to numerical instabilities at the interphase between the star and the atmosphere. In order to prevent that from happening, we add an exponential radial decay of the density profile that smooths the transition to the atmosphere, for densities below a given threshold value $\rho_{\rm thresh,atm}$,

$$\rho(r.\theta) = \max\left(\rho_{\rm thresh,atm}\exp\left[\frac{r - r_{\rm atm}(\theta)}{\Delta_r}\right], \rho_{\rm atm}\right)\,. \tag{31}$$

Table 1. Summary of the initial models. All stars have the same gravitational mass $M_{\rm grav} = 2.60\ {\rm M}_\odot$. The columns report the label of the model, the maximum mass density, $\rho_{\rm max}$, the equatorial radius, $R_{\rm eq}$, the central rotation frequency, Ω_c, the total angular momentum, J, and the strength of the initial poloidal magnetic field, $\bar{b}_0$.

Label	$\rho_{\rm max}$ (10^{14} g cm^{-3})	$R_{\rm eq}$ (km)	Ω_c (s^{-1})	J (10^{48} g cm^2 s^{-1})	$\bar{b}_0$ (10^{13} G)
R1B3	7.90	18.53	2887.85	3.12	7.00
R2B3	7.80	18.58	4922.76	5.32	7.00
R3B3	7.61	18.70	7500.03	8.12	7.00
R3B5	7.61	18.70	7500.03	8.12	10.00
R3B4	7.61	18.70	7500.03	8.12	8.50
R3B2	7.61	18.70	7500.03	8.12	5.00
R3B1	7.61	18.70	7500.03	8.12	3.50

Downloaded from https://academic.oup.com/mnras/article/545/3/staf2081/8340377 by guest on 12 January 2026

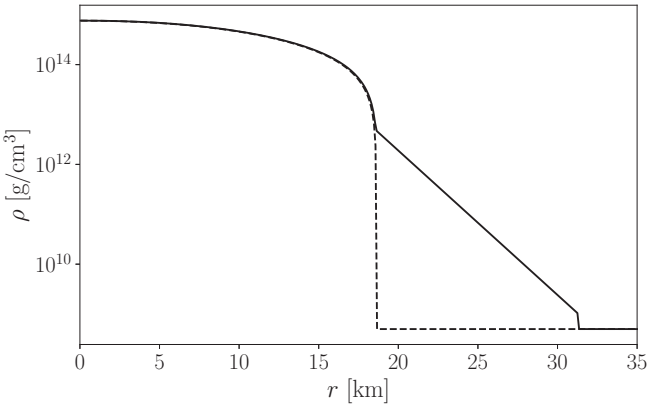

Figure 1. Radial equatorial profile of the initial mass density with (solid line) and without (dashed line) the exponential decay at low values. The profiles are identical for density values above $\rho_{\rm thresh,atm}$.

Both $\rho_{\rm thresh,atm}$ and Δ_r are freely specifiable parameters. The quantity $r_{\rm atm}$ is the radius at which $\rho = \rho_{\rm thresh,atm}$. Fig. 1 shows this density profile (in blue) as compared to that without the exponential decay (indicated by the red curve). Table 1 summarizes our sample of initial models, reporting the maximum mass density, $\rho_{\rm max}$, the equatorial radius, $R_{\rm eq}$, the central rotation frequency, Ω_c, the total angular momentum, J, and the strength of the initial poloidal magnetic field, $\bar{b}_0$. For all models we fix the gravitational mass of the star to $M_{\rm grav} = 2.60\ {\rm M}_\odot$. Moreover, the value of $\rho_{\rm thresh,atm}$ that we employ corresponds to $5 \times 10^{12}\ {\rm g\,cm^{-3}}$, which is more than two orders of magnitude smaller than $\rho_{\rm max}$.

4.2 Numerical evolution

4.2.1 General considerations

The initial models reported in Table 1 are evolved using the AENUS code (M. Obergaulinger 2008) which solves the ideal MHD equations in their conservative form using finite-volume methods. The simulations are performed using the Harten–Lax–van Leer (HLL) flux formula (A. Harten, P. D. Lax & B. v. Leer 1983), a Piecewise Parabolic Method (PPM) reconstruction for cell interfaces (P. Colella & P. R. Woodward 1984), and a third order Runge–Kutta time integrator (C.-W. Shu & S. Osher 1988). For the spatial grid, the code employs spherical polar coordinates (r, θ, ϕ) and axial symmetry with respect to the rotation axis is assumed. The number of grid cells is $(N_r, N_\theta, N_\phi) = (468, 180, 1)$, with $r \in [0, 50]$ km and $\theta \in [0, \pi]$ rad. Since the MInIT coefficients are computed in cylindrical coordinates in M. Miravet-Tenés et al. (2022), a change of basis from cylindrical to spherical coordinates is required. Furthermore, the angular frequency Ω and the shear q are computed from the angular velocity v_ϕ. For the radial direction we use boundary conditions that ensure regularity at the geometric singularity of the origin and employ a constant extrapolation at the outer edge of the grid. Regarding the polar direction, conditions adapted to the polar axis are used.

4.2.2 Implementation of the MInIT model

In order to solve equations (13) and (14), the code employs high-resolution shock-capturing schemes for the transport terms on the left-hand side, as done for the other MHD quantities. As the source terms can be stiff, we treat them in an operator-split manner using an implicit integration, similarly to what O. Just, M. Obergaulinger & H. T. Janka (2015) did to deal with neutrino schemes.

After the transport of angular momentum, the shear parameter q tends to zero in certain regions of the star. Moreover, there might be regions that are not unstable to the MRI, which correspond to the cases with $q < 0$ or $q > 4$ (M. Obergaulinger et al. 2009). For $q < 0$ the fluid is stable and for $q > 4$ the fluid is subject to large-scale shear instabilities, that can be resolved numerically without the need of a subgrid model. As can be seen from equation (18), the MRI wavenumber becomes imaginary for those values of q. For $q \to 0$ and $q \to 4$, the MRI wavelength tends to infinity. This implies that at some value of q close enough to 0 or 4, $\lambda_{\rm MRI} > \Delta$. In such cases, $\lambda_{\rm MRI}$ is replaced by Δ and therefore we substitute $k_{\rm MRI}$ in equation (17) by $k = 2\pi/\Delta$, as done for the turbulent Kolmogorov term in equation (19). Moreover, since the MRI is not expected to develop for $q \leq 0$ and $q \geq 4$, we set $\gamma_{\rm MRI}$ to zero in those cases.

The flattening of the rotational profile of the star as a result of angular momentum transport can also lead to some issues when computing the MRI contribution of the Maxwell stress tensor, since the $\alpha_{ij}^{\rm MRI}$ coefficients depend on $1/q$. To solve this potential issue, we set $\alpha_{ij}^{\rm MRI}$ to zero when $q \leq 10^{-3}$. This should not be problematic, since we expect $e_{\rm MRI}$ and $e_{\rm PI}$ to decay when $q \to 0$.

5 RESULTS

Including turbulent energy densities in the simulations introduces an interplay with large-scale quantities, influencing the evolution of both. In the following we test the impact of different initial values of both large-scale and small-scale quantities on the evolution of the MRI and, consequently, on the large-scale dynamics of the star.

5.1 Dependence on the central rotation frequency

From equations (15) and (17) it follows that the rotation frequency Ω has a direct impact on the growth of the turbulent energy densities of the MInIT model. Fig. 2 depicts the time evolution of the average of these quantities over a sphere of radius $r = 4$ km, for different values of the initial central rotation frequency, given by the models `R1B3`, `R2B3`, and `R3B3` from Table 1. We choose such a low value of r to also depict the turbulence decay, which mainly happens in the central regions of the star. The initial values of $e_{\rm MRI}$ and $e_{\rm PI}$ are chosen to be $10^{-10} e_{\rm kin}(0)$ and $10^{-11} e_{\rm kin}(0)$, respectively. We will

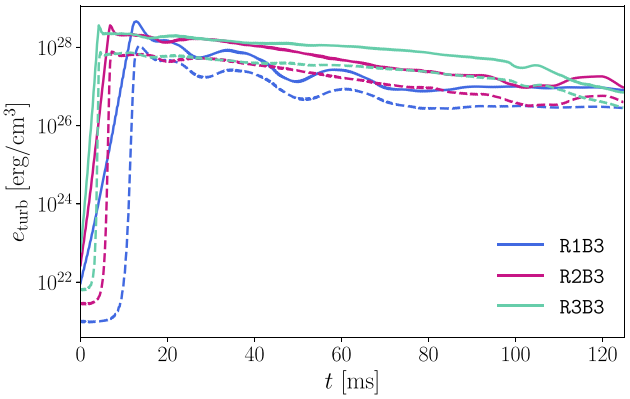

Figure 2. Time evolution of the turbulent energy densities, $e_{\rm MRI}$ (solid lines) and $e_{\rm PI}$ (dashed lines), averaged over a radius of $r = 4$ km. Different colours represent different central initial rotation frequencies.

Downloaded from https://academic.oup.com/mnras/article/545/3/staf2081/8340377 by guest on 12 January 2026

explore in Section 5.3 the impact of different initial values of these quantities on the simulations. To evolve these quantities only at the stellar interior, we set $e_{\rm MRI}(0) = e_{\rm PI}(0) = 0$ for $\rho < 0.1\rho_{\rm max}$, which corresponds to a radius of ~ 17 km, as mentioned before.

As expected, models with larger central rotation frequency, i.e. larger angular momentum, show a more rapid growth of both the MRI and PI energy densities. However, the saturation amplitude of both quantities is approximately the same, regardless of the value of the rotation frequency. Thus, the only difference between the turbulent energy densities for different rotation velocities is the time at which they saturate, which may have an impact on the time-scale of the angular momentum transport. Moreover, after $t \approx 40$ ms, all the saturated turbulent energy densities start decaying, due to the transport of angular momentum that stabilizes the central region of the star against the MRI.

The development of the MRI has an impact on the large-scale dynamics of the NS. In Fig. 3 we showcase the equatorial radial profiles of the angular frequency of the star. Solid lines correspond to simulations that incorporate the MInIT model while dashed lines to those not including it. Quite distinctly, MRI turbulence leads to the flattening of the profile in the inner regions of the star, expanding outwards with time. Hence, the effect of the turbulent stress tensors in the momentum equation is the transport of angular momentum radially outwards. This is observed for all initial models of our sample with different rotation frequencies. Fig. 3 also displays a slight increase of the angular frequency at larger radial distances, where angular momentum is being transported. We note that despite the dashed curves also show a decrease of the central angular frequency, this is purely due to numerical dissipation (see Appendix A for details), and not to the effect of MRI-resolved turbulence. We have checked this by running a simulation with the same spatial resolution but without magnetic fields, observing the same behaviour on the rotational profile.

Fig. 4 shows the contour of the MRI turbulent kinetic energy density, $e_{\rm MRI}$, for the model `R3B3`, at $t = \{2.5, 7.5, 25, 75\}$ ms. There exists a rapid growth during the first 7.5 ms of the simulation, where $e_{\rm MRI}$ grows several orders of magnitude (from $\sim 10^{26}$ to $\sim 10^{29}$ erg cm^{-3} for ϖ up to ~ 10 km). After saturation, and when the redistribution of angular momentum sets in (see Fig. 3) $e_{\rm MRI}$ starts decaying at low values of the cylindrical radial coordinate, ϖ. The cylindrical symmetry is due to the choice of rotation law (see equation 25), which depends on ϖ. The turbulence decay can be understood by looking at Fig. 5, where radial profiles of q are depicted for $t = \{1, 25, 50, 75\}$ ms, as in Fig. 3. As the angular frequency profile flattens, the shear parameter is reduced until the region transitions to rigid rotation, i.e. $q \to 0$. When this happens, the MRI is no longer active in that region and the turbulence generated by this instability can only decay.

5.2 Dependence on the magnetic field strength

We also study the effect of the magnetic field strength on the evolution of the MRI and the PI, and on the global dynamics. We employ three different values of the central poloidal magnetic field, $\bar{b}_0 = \{3.5, 7, 10\} \times 10^{13}$ G, corresponding to the models `R3B1`, `R3B3`, and `R3B5` from Table 1, respectively. It is useful to study the effect of different initial poloidal fields on the evolution of the turbulent energy densities, since the magnetic field explicitly appears in equation (18).

We compare in Fig. 6 the temporal evolution of the turbulent energies using different initial magnetic field strengths, $\bar{b}_0$, and keeping the initial angular frequency from the model `R3B3` and the initial MRI energy density amplitude to $e_{\rm MRI}(0)/e_{\rm kin}(0) = 10^{-10}$,

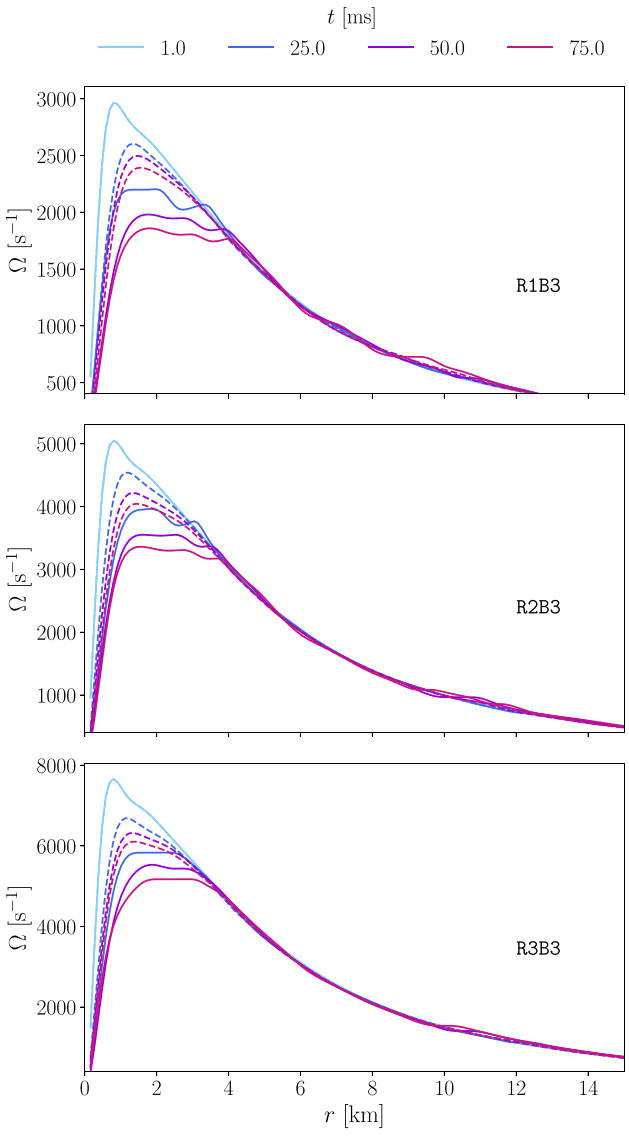

Figure 3. Radial equatorial profiles of the angular frequency, Ω, for several initial central values: 2887.85 Hz (top), 4922.76 Hz (middle), 7500.03 Hz (bottom). Each colour represents different times, indicated in the legend at the top. The solid curves correspond to simulations incorporating the MInIT model while the dashed ones correspond to simulations without it. For $t = 1$ ms, both solid and dashed curves overlap, because the MRI is still developing.

and $e_{\rm PI}(0)/e_{\rm kin}(0) = 10^{-11}$. Although $e_{\rm MRI}$ evolves with the same rate, $e_{\rm PI}$ grows faster for smaller values of $\bar{b}_0$. This is explained by the dependence of the parasitic growth rate from equation (17) with $\bar{b}_0$. The fact that $e_{\rm PI}$ grows faster leads to an earlier saturation of the energy densities at a lower amplitude for $\bar{b}_0 = 3.5 \times 10^{13}$ G. This result is consistent with the findings made by M. Obergaulinger (2008) and T. Rembiasz et al. (2016b), who claimed that the MRI amplification factor, defined as

$$\mathcal{A} \equiv \frac{\sqrt{\bar{M}_{r\phi}(t_{\rm sat})}}{\bar{b}_0}\,, \tag{32}$$

has a very weak dependence on the initial poloidal magnetic field. This translates in a linear dependence between $\sqrt{\bar{M}_{r\phi}(t_{\rm sat})}$ and $\bar{b}_0$, as depicted in Fig. 7. In this case, we show the maximum values of the square root of the averaged $r\phi$ component from the Maxwell stress

Downloaded from https://academic.oup.com/mnras/article/545/3/staf2081/8340377 by guest on 12 January 2026

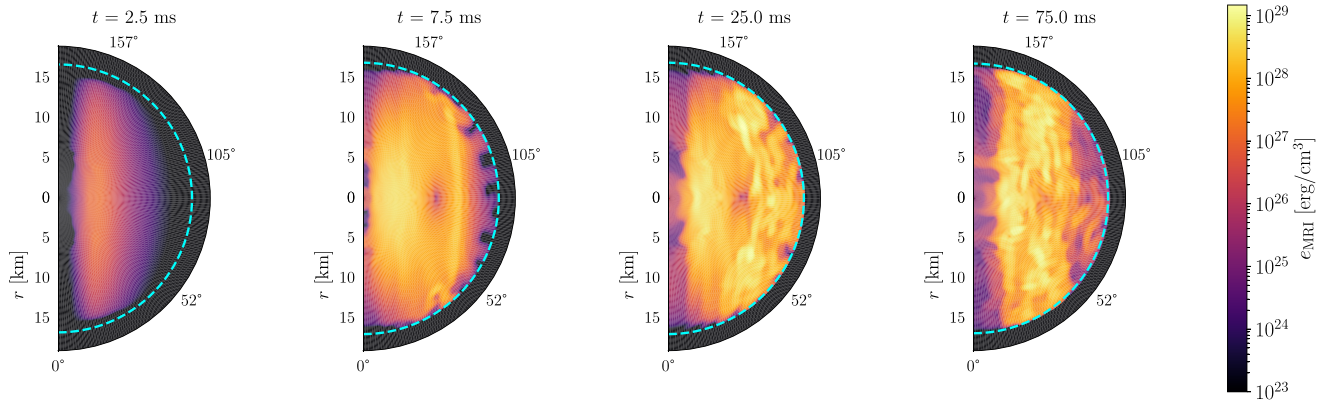

Figure 4. Contour plot of the turbulent kinetic energy density of the MRI, $e_{\rm MRI}$. Each panel stands for different times $t = \{2.5, 7.5, 25, 75\}$ ms. After a rapid growth during the first $\sim$ 10 ms through all the stellar domain, the energy density starts decaying at the inner region of the star, due to the transport of angular momentum from the centre. The blue dashed line stands for the isocontour of the mass density ρ at 10 per cent of its central value.

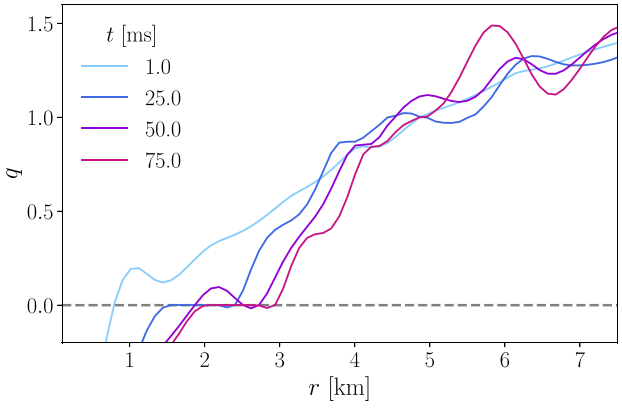

Figure 5. Radial equatorial profiles of the shear parameter at different times, corresponding to the simulation labelled with `R3B3`. Due to angular momentum transport, q tends to 0 (dashed line) as time increases.

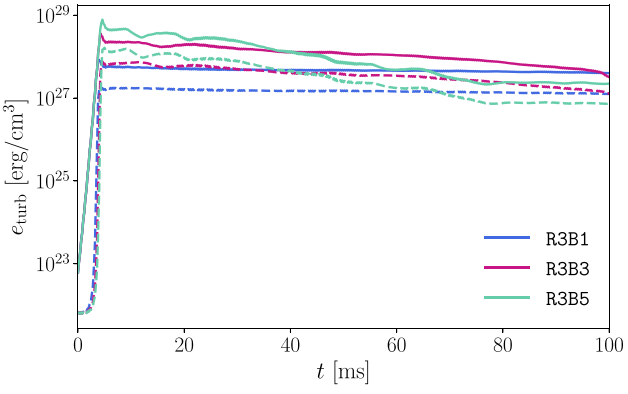

Figure 6. Time evolution of the turbulent energy densities, $e_{\rm MRI}$ (solid) and $e_{\rm PI}$ (dashed) averaged over a radius of $r = 4$ km. We depict simulations with different initial poloidal magnetic field amplitudes at the centre of the star. The central initial rotation frequency is fixed to 7500.03 Hz.

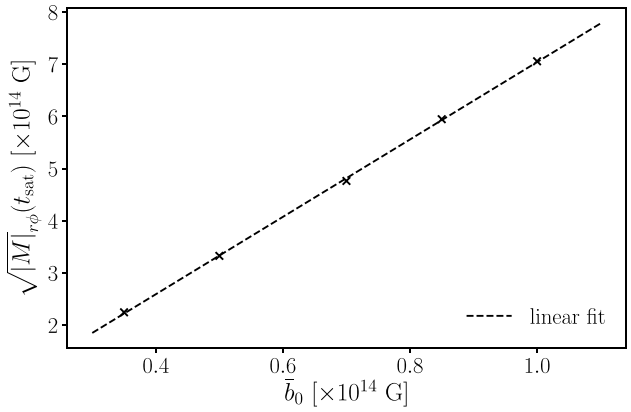

Figure 7. Absolute values at saturation of the square root of the $r\phi$ component of the Maxwell stress tensor, averaged over a radius of $r = 8$ km, as a function of the initial poloidal field amplitude. The crosses stand for the saturated values from simulations `R3B1`, `R3B2`, `R3B3`, `R3B4`, and `R3B5`. The dashed line represents the linear fit.

tensor, over a radius of $r = 8$ km, for five different values of the initial poloidal magnetic field (see Table 1). These maximum values clearly grow linearly with the poloidal field amplitude, $\bar{b}_0$. In Fig. 8 we see the impact of the different choices of the initial magnetic field on the angular frequency of the NS. It can be seen that, after the first $\sim$ 10 ms, the maximum value of the equatorial angular frequency, $\Omega_{\rm max}$, starts decaying faster in those simulations with a larger poloidal magnetic field, once the MRI reaches its largest amplitude. We note that the oscillations in the central rotation frequency at early times are due to the inclusion of the exponential decay of the density profile, which alters the equilibrium state of the NS. Even though there is a slight decay of $\Omega_{\rm max}$ in the simulations without the MInIT model (grey lines) due to numerical dissipation (see Appendix A), this decay is much less pronounced than the rest of simulations which include the subgrid model. As mentioned above, since we have not included the subgrid terms in the induction equation, we do not expect any large-scale magnetic field amplification triggered by the MRI dynamo. Therefore, the poloidal magnetic field, which is the

Downloaded from https://academic.oup.com/mnras/article/545/3/staf2081/8340377 by guest on 12 January 2026

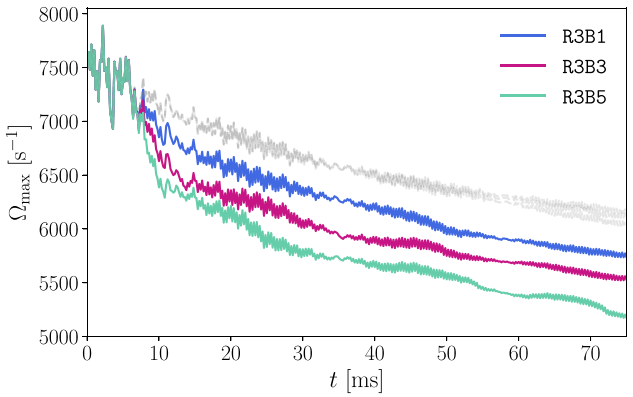

Figure 8. Time evolution of the maximum value of the angular frequency for simulations with the MInIT model that have different initial poloidal magnetic field amplitudes. The grey overlapping lines depict the results from the same three simulations without including the MInIT model.

component entering in equations (13) and (14) through $\gamma_{\rm PI}$, remains nearly constant during the simulation.

5.3 Dependence on the initial amplitudes of the turbulent energy densities

We have the freedom to choose the initial value of the turbulent energy densities, $e_{\rm MRI}(0)$ and $e_{\rm PI}(0)$. The growth time-scale and saturation amplitude of the MRI might also be sensitive to the choice of these quantities. From the local analytical results from M. Miravet-Tenés & M. E. Pessah (2025) and the numerical results from T. Rembiasz et al. (2016b), we should not expect a noticeable difference in the saturation amplitude of the instability. To test this, we employ simulation `R3B3` from Table 1 with different choices of $e_{\rm MRI}(0)$ and $e_{\rm PI}(0)$, expressed as a fraction of the initial large-scale kinetic energy density, $e_{\rm kin}(0)$.

Fig. 9 depicts the time evolution of the turbulent energy densities for different initial amplitudes. The left panel shows different choices of $e_{\rm MRI}(0)$, fixing $e_{\rm PI}(0)$ at $10^{-11}e_{\rm kin}(0)$, whereas in the right panel we keep $e_{\rm MRI}(0)$ fixed at $10^{-7}e_{\rm kin}(0)$. We can observe in the left panel that choosing a different value of $e_{\rm MRI}(0)$ leads to a different saturation time. Larger values of the initial MRI energy density lead to a more rapid growth of the parasitic energy density and therefore to an earlier saturation. Nevertheless, the saturation amplitude of the MRI remains mostly insensitive to the choice of $e_{\rm MRI}(0)$. In the right panel of Fig. 9 we see that simulations employing different values of $e_{\rm PI}(0)$ saturate at almost the same time. The maximum MRI amplitude is slightly different (larger for lower amplitudes of the initial parasitic energy density, cf. M. Miravet-Tenés & M. E. Pessah 2025), but after saturation all simulations reach the same MRI and PI values. These results lead to the conclusion that, assuming that the turbulent energy densities should be several orders of magnitude smaller than the large-scale kinetic energy density, the choice of their initial values should not have an important impact on the large-scale dynamics.

6 DISCUSSION

The lack of spatial resolution in current numerical simulations of BNS mergers (and core–collapse supernovae) prevents the development of the MRI during the post-merger phase. This undermines the credibility of the simulations as the MRI can play a crucial role in the evolution of the remnant. Angular momentum transport drives the system toward rigid rotation, at which point the HMNS is expected to collapse into a black hole. The characteristic time-scale for angular momentum transport is estimated to be of $\mathcal{O}(100)$ ms, though it depends on the remnant's rotational profile (K. Hotokezaka et al. 2013). Hence, the BNS remnant is expected to undergo collapse to a black hole within roughly $\mathcal{O}(100)$ ms after merger, although in extreme cases, collapse can also occur much earlier. This time-scale has direct implications for the associated kilonova that produces r-process nucleosynthesis, which powers electromagnetic emission. Moreover, the collapse of the HMNS is required for the launch of a GRB (e.g. M. Ruiz et al. 2016; A. Murguia-Berthier et al. 2017), meaning that accurate simulations capable of reliably capturing the lifetime of the remnant are essential for interpreting gamma-ray detections from such mergers. Conversely, simulations that fail to incorporate turbulent effects may produce artificially long-lived remnants that cannot generate sufficiently powerful outflows to drive a GRB.

The use of LES can help capture the impact of the small-scale turbulence on the overall dynamics of the system. In this work we have presented results from simulations of differentially

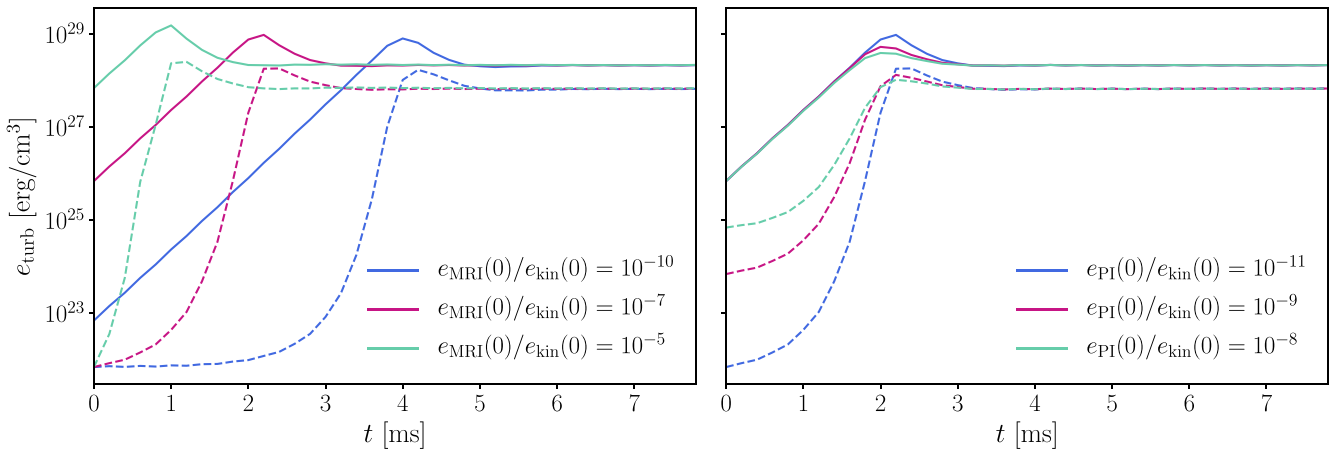

Figure 9. Time evolution of the turbulent energy densities, $e_{\rm MRI}$ (solid) and $e_{\rm PI}$ (dashed) averaged over a radius of $r = 8$ km. We show different choices of the initial turbulent energy densities, $e_{\rm MRI}(0)$ and $e_{\rm PI}(0)$. In the left panel we keep $e_{\rm PI}(0)$ fixed to $10^{-11}e_{\rm kin}(0)$, whereas in the right panel we set $e_{\rm MRI}(0) = 10^{-7}e_{\rm kin}(0)$. In all cases, we use the same initial data as in simulation `R3B3` from Table 1.

Downloaded from https://academic.oup.com/mnras/article/545/3/staf2081/8340377 by guest on 12 January 2026

rotating, magnetized NSs including the MInIT subgrid model we first presented in M. Miravet-Tenés et al. (2022). With the addition of the evolution equations of the turbulent energy densities for the MRI and the PI from the MInIT model, we have been able to compute the turbulent stress tensors responsible for turbulent angular momentum transport, i.e. the Maxwell and Reynolds stresses. We have observed that their inclusion in the momentum equation of the fluid has an impact on the global dynamics of the NS, leading to a net transport of angular momentum radially outwards, which reduces the rotation frequency of the star in its central regions. Moreover, in the regions where the rotational profile flattens, the turbulent energy densities and therefore the turbulent stresses, decay, as one would expect when the fluid loses its differential rotation.

Our results show that the evolution of the turbulent energy densities is sensitive to the rotation frequency of the star and to the strength of the poloidal magnetic field. Although the saturation amplitude of the energies is very similar, different choices of the central rotation frequency of the NS lead to different growth rates of the MRI, which results in different saturation times. Regarding the amplitude of the initial magnetic field, its choice has a direct impact on the growth of the PI, resulting in a larger parasitic growth rate for lower magnetic field amplitudes. Thus, stronger poloidal fields lead to a larger saturation amplitude, as previously noted by T. Rembiasz et al. (2016a, b) and M. Miravet-Tenés & M. E. Pessah (2025), which in turn produces a more effective angular momentum transport.

The MInIT model also needs a value of the initial amplitudes of the turbulent energies. Assuming that these quantities will be a small fraction of the initial large-scale kinetic energy, we have performed several simulations with different choices of these initial values. Although they impact the saturation time of the instability, the saturation amplitude remains the same. Therefore, the effect of the choice of the initial amplitude of the turbulent energies on the growth of the MRI is somewhat similar to that produced by different values of the central rotation frequency of the NS. One might think this could be an issue, since $e_{\rm MRI}(0)$ and $e_{\rm PI}(0)$ are free parameters of the model. Nevertheless, their impact is fairly low as this just delays saturation by a few milliseconds.

It is important to point out that this work should be regarded as a promising test of the MInIT model in global simulations of isolated NSs. However, there are a number of assumptions that should be relaxed in future work. On the one hand, the setup of the simulations is far from being realistic: we enforced axisymmetry, employed Newtonian dynamics, used a cold polytropic EOS with an ideal-gas-like part for the thermal contribution, and adopted a rotation law which, although widely employed in the literature, departs from those inferred from simulations for BNS merger remnants (M. Hanauske et al. 2017; P. Iosif & N. Stergioulas 2022; M. Cassing & L. Rezzolla 2024). Those are all aspects that need to be considered in future applications of the model. Furthermore, the most immediate step to make to improve the model is the implementation of the Faraday stress tensor in the induction equation for the magnetic field, which might induce an effective dynamo. This could also have an impact on the evolution of the MRI itself after saturation. In addition, it would be advisable to conduct a comparison between low-resolution simulations including the MInIT model and high-resolution simulations able to capture the MRI unaided by a subgrid model, and in three dimensions. In this regard we note that since our simulations are axisymmetric, the associated MRI would be quantitatively different from the one expected in 3D (M. Obergaulinger et al. 2009), which is the one used to calibrate the MInIT model in M. Miravet-Tenés et al. (2022). However, in order to run a 3D simulation that fully resolves the MRI, we would need enough spatial resolution to cover at least 10 grid cells per MRI wavelength. As an illustrative example, the simulation `R3B3`, with $\bar{b}_0 = 7 \times 10^{13}$ G, has a radial resolution of 107 m, whereas $\lambda_{\rm MRI}$ is found to be ~ 10 m through almost the whole stellar interior. The total CPU time of the simulation was ≈ 300 h. To fully resolve the MRI in 3D, we would need to add the azimuthal dimension and increase the resolution by a factor 100 in each direction, which would increase the CPU time by a factor $\sim 10^8$, requiring $\sim 10^6$ yr of CPU time.

Finally, the use of Newtonian physics and dynamics is a major limitation of our current approach. In BNS mergers (and also core–collapse supernovae) the space–time metric deviates strongly from the flat metric, and the fluid velocity can become relativistic in some regions. Therefore, a more realistic approach would be the performance of fully general-relativistic LES, as done in, e.g. B. Giacomazzo et al. (2015), D. Radice (2020), C. Palenzuela et al. (2022), and R. Aguilera-Miret et al. (2025). Nevertheless, most of these works solely focus on the turbulent magnetic field amplification by the KHI and are unable to capture the effects of the MRI in the post-merger phase. Moreover, they lack the ability to handle the dependence of the saturation amplitude on the magnetic field amplitude, the relation between the rotation frequency and the growth phase, or the decay of turbulence in MRI-stable regions. Another key issue is that subgrid models applied to GRMHD simulations of BNS mergers are covariant with respect to transformations in the spatial coordinates, but not when it comes to general space–time coordinate transformations (M. D. Duez et al. 2020; D. Radice & I. Hawke 2024). Non-covariant closures can introduce coordinate-independent artefacts in the simulations, since the averaging applied to a single foliation can inherit the dependencies of that space–time slice. For that purpose, it is important to develop a covariant approach (M. D. Duez et al. 2020; T. Celora et al. 2021, 2024a, b) that would allow the MInIT model to be used in general–relativistic simulations. We plan to report on those extensions of the model in future work.

ACKNOWLEDGEMENTS

This work has been supported by the Spanish Agencia Estatal de Investigación (grants PID2021-125485NB-C21 and PID2024-159689NB-C21) funded by MCIN/AEI/10.13039/501100011033 and ERDF A way of making Europe, and by the Prometeo excellence programme grants CIPROM/2022/13 and CIPROM/2022/49 funded by the Generalitat Valenciana. MMT acknowledges support from the Science and Technology Facilities Council (STFC), via grant No. ST/Y000811/1, and from the Ministerio de Ciencia, Innovación y Universidades del Gobierno de España through the 'Ayuda para la Formación de Profesorado Universitario' (FPU) fellowship No. FPU19/01750. MO was supported by the Ramón y Cajal programme of the Agencia Estatal de Investigación (RYC2018-024938-I). MR acknowledges support by the Generalitat Valenciana grant CIDEGENT/2021/046. We acknowledge further support from the European Horizon Europe Staff Exchanges (SE) programme HORIZON-MSCA2021-SE-01 Grant No. NewFunFiCO-101086251.

This work has used the following open-source packages: NUMPY (C. R. Harris et al. 2020), SCIPY (P. Virtanen et al. 2020), H5PY (A. Collette et al. 2023), and MATPLOTLIB (J. D. Hunter 2007).

DATA AVAILABILITY

The data underlying this article will be shared on reasonable request to the corresponding author.

Downloaded from https://academic.oup.com/mnras/article/545/3/staf2081/8340377 by guest on 12 January 2026

REFERENCES

Abbott B. P. et al., 2017a, Nature, 551, 85
Abbott B. P. et al., 2017b, ApJ, 848, L12
Abbott B. P. et al., 2017c, ApJ, 848, L13
Aguilera-Miret R., Viganò D., Palenzuela C., 2022, ApJ, 926, L31
Aguilera-Miret R., Christian J.-E., Rosswog S., Palenzuela C., 2025, MNRAS, 542, 3067
Akiyama S., Wheeler J. C., Meier D. L., Lichtenstadt I., 2003, ApJ, 584, 954
Anderson M., Hirschmann E. W., Lehner L., Liebling S. L., Motl P. M., Neilsen D., Palenzuela C., Tohline J. E., 2008, Phys. Rev. Lett., 100, 191101
Balbus S. A., Hawley J. F., 1991, ApJ, 376, 214
Balbus S. A., Hawley J. F., 1992, ApJ, 392, 662
Balbus S. A., Hawley J. F., 1998, Rev. Mod. Phys., 70, 1
Baumgarte T. W., Shapiro S. L., Shibata M., 2000, ApJ, 528, L29
Bauswein A., Baumgarte T. W., Janka H. T., 2013, Phys. Rev. Lett., 111, 131101
Bernuzzi S., 2020, Gen. Relativ. Gravit., 52, 108
Cassing M., Rezzolla L., 2024, MNRAS, 532, 945
Celora T., Andersson N., Hawke I., Comer G. L., 2021, Phys. Rev. D, 104, 084090
Celora T., Andersson N., Hawke I., Comer G. L., Hatton M. J., 2024a, Phys. Rev. D, 110, 123039
Celora T., Hatton M. J., Hawke I., Andersson N., 2024b, Phys. Rev. D, 110, 123040
Cerdá-Durán P., Font J. A., Antón L., Müller E., 2008, A&A, 492, 937
Chandrasekhar S., 1960, Proc. Natl Acad. Sci., 46, 253
Charbonneau P., 2013, Solar and Stellar Dynamos (Saas-Fee Advanced Course). Springer, Berlin
Chou P. Y., 1945, Quart. Appl. Math., 3, 38
Ciolfi R., Kastaun W., Kalinani J. V., Giacomazzo B., 2019, Phys. Rev. D, 100, 023005
Colella P., Woodward P. R., 1984, J. Comput. Phys., 54, 174
Collette A. et al., 2023, h5py/h5py: 3.8.0. Zenodo
Dimmelmeier H., Font J. A., Muller E., 2002, A&A, 388, 917
Duez M. D., Liu Y. T., Shapiro S. L., Stephens B. C., 2004, Phys. Rev. D, 69, 104030
Duez M. D., Liu Y. T., Shapiro S. L., Shibata M., Stephens B. C., 2006, Phys. Rev. D, 73, 104015
Duez M. D. et al., 2020, Phys. Rev. D, 102, 104050
Eichler D., Livio M., Piran T., Schramm D. N., 1989, Nature, 340, 126
Espino P. L., Paschalidis V., 2019, Phys. Rev. D, 99, 083017
Etienne Z. B., Liu Y. T., Paschalidis V., Shapiro S. L., 2012, Phys. Rev. D, 85, 064029
Giacomazzo B., Zrake J., Duffell P. C., MacFadyen A. I., Perna R., 2015, ApJ, 809, 39
Goodman J., Xu G., 1994, ApJ, 432, 213
Hammond P., Hawke I., Andersson N., 2021, Phys. Rev. D, 104, 103006
Hanauske M., Takami K., Bovard L., Rezzolla L., Font J. A., Galeazzi F., Stöcker H., 2017, Phys. Rev. D, 96, 043004
Harris C. R. et al., 2020, Nature, 585, 357
Harten A., Lax P. D., Leer B. v., 1983, SIAM Rev., 25, 35
Hotokezaka K., Kiuchi K., Kyutoku K., Muranushi T., Sekiguchi Y.-i., Shibata M., Taniguchi K., 2013, Phys. Rev. D, 88, 044026
Hunter J. D., 2007, Comput. Sci. Eng., 9, 90
Iosif P., Stergioulas N., 2022, MNRAS, 510, 2948
Izquierdo M. R., Bezares M., Liebling S., Palenzuela C., 2024, Phys. Rev. D, 110, 083017
Janka H. T., Zwerger T., Moenchmeyer R., 1993, A&A, 268, 360
Just O., Obergaulinger M., Janka H. T., 2015, MNRAS, 453, 3386
Kastaun W., Galeazzi F., 2015, Phys. Rev. D, 91, 064027
Kawamura T., Giacomazzo B., Kastaun W., Ciolfi R., Endrizzi A., Baiotti L., Perna R., 2016, Phys. Rev. D, 94, 064012
Kiuchi K., Kyutoku K., Sekiguchi Y., Shibata M., Wada T., 2014, Phys. Rev. D, 90, 041502
Kiuchi K., Cerdá-Durán P., Kyutoku K., Sekiguchi Y., Shibata M., 2015, Phys. Rev. D, 92, 124034
Kiuchi K., Kyutoku K., Sekiguchi Y., Shibata M., 2018, Phys. Rev. D, 97, 124039
Kiuchi K., Reboul-Salze A., Shibata M., Sekiguchi Y., 2024, Nat. Astron., 8, 298
Komatsu H., Eriguchi Y., Hachisu I., 1989, MNRAS, 237, 355
Krause F., Rädler K., 1980, Mean-Field Magnetohydrodynamics and Dynamo Theory. Pergamon Press, Oxford
Landau L. D., Lifshitz E. M., 1987, Fluid Mechanics. Pergamon, Oxford
Latter H. N., Lesaffre P., Balbus S. A., 2009, MNRAS, 394, 715
Lesaffre P., Balbus S. A., Latter H., 2009, MNRAS, 396, 779
Li L.-X., Paczynski B., 1998, ApJ, 507, L59
Liu Y. T., Shapiro S. L., Etienne Z. B., Taniguchi K., 2008, Phys. Rev. D, 78, 024012
MacFadyen A. I., Woosley S. E., 1999, ApJ, 524, 262
Margalit B., Metzger B. D., 2017, ApJ, 850, L19
Margalit B., Jermyn A. S., Metzger B. D., Roberts L. F., Quataert E., 2022, ApJ, 939, 51
Metzger B. D. et al., 2010, MNRAS, 406, 2650
Miravet-Tenés M., Pessah M. E., 2025, A&A, 696, A2
Miravet-Tenés M., Cerdá-Durán P., Obergaulinger M., Font J. A., 2022, MNRAS, 517, 3505
Miravet-Tenés M., Cerdá-Durán P., Obergaulinger M., Font J. A., 2024, MNRAS, 527, 1081
Murguia-Berthier A. et al., 2017, ApJ, 835, L34
Nissanke S., Holz D. E., Hughes S. A., Dalal N., Sievers J. L., 2010, ApJ, 725, 496
Obergaulinger M., 2008, PhD thesis, Max-Planck-Institute for Astrophysics, Garching
Obergaulinger M., Aloy M. A., Dimmelmeier H., Müller E., 2006, A&A, 457, 209
Obergaulinger M., Cerdá-Durán P., Müller E., Aloy M. A., 2009, A&A, 498, 241
Palenzuela C., Aguilera-Miret R., Carrasco F., Ciolfi R., Kalinani J. V., Kastaun W., Miñano B., Viganò D., 2022, Phys. Rev. D, 106, 023013
Perego A., Bernuzzi S., Radice D., 2019, Eur. Phys. J. A, 55, 124
Pessah M. E., 2010, ApJ, 716, 1012
Pessah M. E., Chan C.-k., 2008, ApJ, 684, 498
Pessah M. E., Goodman J., 2009, ApJ, 698, L72
Pessah M. E., Chan C.-K., Psaltis D., 2006, MNRAS, 372, 183
Piro A. L., Giacomazzo B., Perna R., 2017, ApJ, 844, L19
Radice D., 2020, Symmetry, 12, 1249
Radice D., Hawke I., 2024, Living Rev. Comput. Astrophys., 10, 1
Reboul-Salze A., Guilet J., Raynaud R., Bugli M., 2021, A&A, 645, A109
Rembiasz T., Obergaulinger M., Cerdá-Durán P., Müller E., Aloy M. A., 2016a, MNRAS, 456, 3782
Rembiasz T., Guilet J., Obergaulinger M., Cerdá-Durán P., Aloy M. A., Müller E., 2016b, MNRAS, 460, 3316
Reynolds O., 1895, Phil. Trans. R. Soc. London Ser. A, 186, 123
Rezzolla L., Most E. R., Weih L. R., 2018, ApJ, 852, L25
Ruiz M., Lang R. N., Paschalidis V., Shapiro S. L., 2016, ApJ, 824, L6
Ruiz M., Shapiro S. L., Tsokaros A., 2018, Phys. Rev. D, 97, 021501
Ruiz M., Tsokaros A., Shapiro S. L., 2021, Phys. Rev. D, 104, 124049
Sarin N., Lasky P. D., 2021, Gen. Relativ. Gravit., 53, 59
Schutz B. F., 1986, Nature, 323, 310
Shapiro S. L., 2000, ApJ, 544, 397
Shibata M., 2015, Numerical Relativity. World Scientific, Singapore. Available at: https://www.worldscientific.com/doi/pdf/10.1142/9692
Shibata M., Sekiguchi Y.-I., 2005, Phys. Rev. D, 72, 044014
Shibata M., Duez M. D., Liu Y. T., Shapiro S. L., Stephens B. C., 2006, Phys. Rev. Lett., 96, 031102
Shibata M., Fujibayashi S., Hotokezaka K., Kiuchi K., Kyutoku K., Sekiguchi Y., Tanaka M., 2017, Phys. Rev. D, 96, 123012
Shu C.-W., Osher S., 1988, J. Comput. Phys., 77, 439
Siegel D. M., Ciolfi R., Harte A. I., Rezzolla L., 2013, Phys. Rev. D, 87, 121302
Suwa Y., Takiwaki T., Kotake K., Sato K., 2007, PASJ, 59, 771

Downloaded from https://academic.oup.com/mnras/article/545/3/staf2081/8340377 by guest on 12 January 2026

Velikhov E. P., 1959, Sov. J. Exp. Theor. Phys., 9, 995
Virtanen P. et al., 2020, Nat. Methods, 17, 261
Weih L. R., Most E. R., Rezzolla L., 2018, MNRAS, 473, L126
Zwerger T., Mueller E., 1997, A&A, 320, 209

APPENDIX A: NUMERICAL DISSIPATION

The discretization of partial differential equations for numerical solutions inevitably introduces numerical dissipation, which affects the evolution of the system. This phenomenon is well understood and, among other consequences, leads to a reduction in kinetic energy. As illustrated in Fig. 8, numerical dissipation may also explain the reduction in the maximum rotation frequency observed in MHD simulations that exclude MInIT (grey lines).

To test this hypothesis, we performed two additional simulations with finer spatial resolutions: `Res2`, with a grid $(N_r, N_\theta, N_\phi) = (576, 252, 1)$, and `Res3`, with (720,360,1). For comparison, we also include the baseline simulation already used in this work, `R3B3` (labelled here as `Res1`), with $(N_r, N_\theta, N_\phi) = (468, 180, 1)$. Fig. A1 demonstrates that higher spatial resolution reduces the decline of the maximum equatorial angular frequency over time. However, a decay remains, indicating that kinetic energy is still dissipated through grid discretization. The time evolution of $\Omega_{\rm max}$ is qualitatively consistent across all runs, with maximum relative differences of ~ 3 per cent between `Res2` and `Res3`, and ~ 5 per cent between `Res1` and `Res3`.

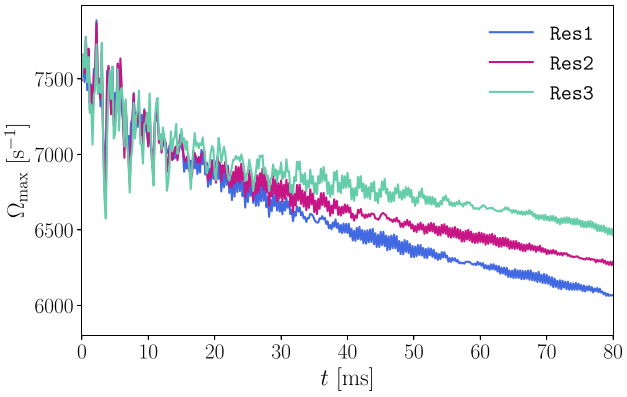

Figure A1. Time evolution of the maximum value of the angular frequency, $\Omega_{\rm max}$, at the equator for the simulation `R3B3`, with three different spatial resolutions. The simulation with the largest resolution, `Res3`, shows a slower decay of $\Omega_{\rm max}$ compared to the simulations with a lower resolution.

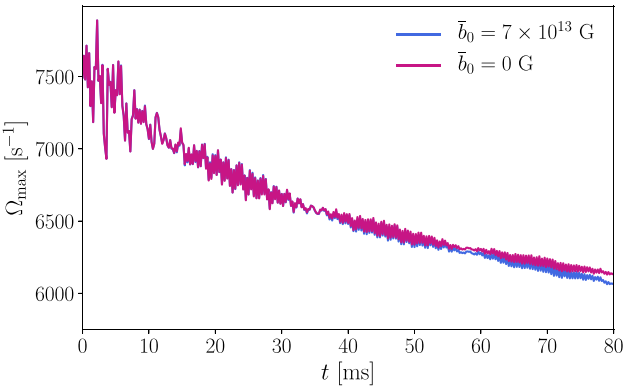

Figure A2. Time evolution of the maximum value of the angular frequency, $\Omega_{\rm max}$, at the equator for the simulation `R3B3`, with (blue) and without (red) magnetic fields. The evolution is identical in both cases, except for late times ($t > 60$ ms), where the higher numerical viscosity of the magnetized case leads to a larger decay of $\Omega_{\rm max}$.

A fully convergent simulation with negligible numerical dissipation would show no decrease in $\Omega_{\rm max}$. In practice, however, the limited resolution and the out-of-equilibrium initial conditions (arising from modified density profiles) prevent complete convergence. Still, the small relative differences across resolutions give us confidence that the results from `Res1` remain qualitatively robust.

One could argue that the decrease in $\Omega_{\rm max}$ might have a physical origin, perhaps due to the action of a partially resolved MRI. This is excluded by construction: the chosen spatial resolution ensures that the cell size is roughly ten times larger than the wavelength of the fastest growing MRI mode, $\lambda_{\rm MRI} = 2\pi/k_{\rm MRI}$ (see equation 18). We further confirm this by performing a simulation without magnetic fields. In Fig. A2, we show the equatorial time evolution of $\Omega_{\rm max}$ for simulation `R3B3` from Table 1, both with (blue) and without (red) magnetic fields. The two curves are indistinguishable up to $t \approx 60$ ms, when they diverge slightly. This minor discrepancy arises because numerical viscosity is generally higher in MHD simulations than in purely hydrodynamical ones.

This paper has been typeset from a TEX/LATEX file prepared by the author.

Downloaded from https://academic.oup.com/mnras/article/545/3/staf2081/8340377 by guest on 12 January 2026

© The Author(s) 2025.
Published by Oxford University Press on behalf of Royal Astronomical Society. This is an Open Access article distributed under the terms of the Creative Commons Attribution License (https://creativecommons.org/licenses/by/4.0/), which permits unrestricted reuse, distribution, and reproduction in any medium, provided the original work is properly cited.